
This is an electronic reprint of the original article.
This reprint may differ from the original in pagination and typographic detail.

Wang, Zulin; Yliniemi, Kirsi; Rautama, Eeva-Leena; Hannula, Pyry-Mikko; Wilson, Benjamin P.; Lundström, Mari

Electrochemical Growth of Ag/Zn Alloys from Zinc Process Solutions and Their Dealloying Behavior

Published in:
ACS Sustainable Chemistry and Engineering

DOI:
[10.1021/acssuschemeng.2c00284](https://doi.org/10.1021/acssuschemeng.2c00284)

Published: 21/03/2022

Document Version
Publisher's PDF, also known as Version of record

Published under the following license:
CC BY

Please cite the original version:
Wang, Z., Yliniemi, K., Rautama, E.-L., Hannula, P.-M., Wilson, B. P., & Lundström, M. (2022). Electrochemical Growth of Ag/Zn Alloys from Zinc Process Solutions and Their Dealloying Behavior. *ACS Sustainable Chemistry and Engineering*, 10(11), 3716–3725. <https://doi.org/10.1021/acssuschemeng.2c00284>

This material is protected by copyright and other intellectual property rights, and duplication or sale of all or part of any of the repository collections is not permitted, except that material may be duplicated by you for your research use or educational purposes in electronic or print form. You must obtain permission for any other use. Electronic or print copies may not be offered, whether for sale or otherwise to anyone who is not an authorised user.

Electrochemical Growth of Ag/Zn Alloys from Zinc Process Solutions and Their Dealloying Behavior

Zulin Wang, Kirsi Yliniemi, Eeva-Leena Rautama, Pyry-Mikko Hannula, Benjamin P. Wilson, and Mari Lundström*



Cite This: *ACS Sustainable Chem. Eng.* 2022, 10, 3716–3725



Read Online

ACCESS |



Metrics & More



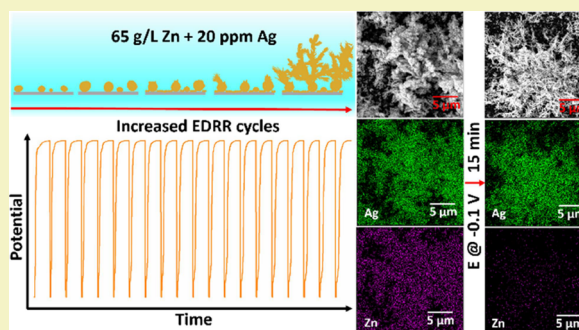
Article Recommendations



Supporting Information

ABSTRACT: This study investigates the sustainable preparation of Ag/Zn alloys from a simulated zinc process solution (20 ppm Ag, 65 g/L Zn, and 10 g/L H₂SO₄) via electrodeposition-redox replacement (EDRR) and the electrochemical dealloying behavior of the Ag/Zn alloys. Results indicate that Ag/Zn deposits with diverse compositions and microstructures can be obtained at room temperature without any complexing agents, simply by varying EDRR parameters like deposition time, deposition potential, and redox replacement time. Two types of Ag/Zn intermetallics (Zn_{0.96}Ag_{0.04} and Ag_{0.76}Zn_{0.24}) were identified by the combination of X-ray diffraction (XRD) and anodic linear sweep voltammetry. Mass-transfer limitations have significant effects on the growth process, and a nucleation-growth mechanism from Ag/Zn particles into dendrites with increased EDRR cycles is introduced: with EDRR parameters favoring mass-transfer limitations (higher overpotentials, longer deposition times, and shorter redox replacement times), a more dendritic morphology of Ag/Zn alloys is achieved. The selective dissolution of Zn (i.e. dealloying) allowed the formation of silver-rich surfaces with an enhanced surface plasmon resonance behavior, which can be readily tuned by EDRR and dealloying parameters. These results highlight the significant potential of the EDRR-dealloying route to produce different types of Ag/Zn alloys and optically functional materials directly from base metal process solutions.

KEYWORDS: EDRR, dendrite, circular economy, crystal growth, optical properties



INTRODUCTION

Silver-based bimetallic functional materials such as nanoparticles and anisotropic nanostructures have been used in various areas like catalysts,¹ sensors,² solar cells,³ and antimicrobial materials⁴ because of their superior properties. Traditionally, the preparation of these materials has relied on the usage of high-purity silver sources and strictly controlled experimental conditions. However, the supply of silver currently faces the twin challenges of increased silver consumption, whilst there is a concurrent depletion in the availability of high-grade raw materials.⁵ To realize sustainable development concepts, the further exploitation of secondary raw materials as metal sources for functional material production has attracted great attention.^{6–8} In contrast, precious metals [like Au, Ag, and platinum group metals (PGMs)] widely present in hydrometallurgical process solutions of base metals (Zn, Cu, Ni, and so forth) have been underutilized as typical sources for functional material production because of their minute concentrations (ppm level or lower).^{9–12} The recent innovation of the electrodeposition-redox replacement (EDRR) method has been found to be a promising approach for metal recovery from extremely low concentration solutions.^{13–22} Moreover, because of its

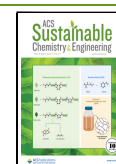
capability to control the resultant product properties, the EDRR approach also has significant potential for streamlining the traditional manufacturing routes by directly preparing high value-added functional surfaces from process and waste solutions. For example, the feasibility of the direct preparation of Pt/Ni,²³ Ag/Cu,²⁴ and Ag/Zn²⁵ bimetallic particles from different hydrometallurgical solutions has been demonstrated.

The Ag/Zn pair is attractive not only because of its wide range of application potential like photocatalysis,²⁶ antimicrobial surfaces,²⁷ and CO₂ reduction²⁸ but also because it reduces the consumption of silver from primary resources. Additionally, Ag/Zn alloys can be used as the templates for the preparation of porous Ag-rich materials for various applications.^{29–33} Traditionally, Ag and Zn have been combined using smelting–casting and electrodeposition. Among these, the smelting–casting process requires significant investment for

Received: January 14, 2022

Revised: February 28, 2022

Published: March 7, 2022



high-temperature furnaces and milling facilities to mix high-purity Ag and Zn powders,^{29–33} whereas electrodeposition involves the reduction of Ag and Zn ions from liquid solutions and can be performed at room temperature.^{34–38} Nevertheless, because of the significant potential difference (1.56 V) between of Ag⁺/Ag (E^0 (standard potential) = +0.15 V vs Hg/Hg₂SO₄) and Zn²⁺/Zn (E^0 = −1.41 V vs Hg/Hg₂SO₄) redox pairs, traditional electrodeposition requires the addition of complexing agents like cyanides, ethylenediaminetetraacetic acid (EDTA), or thiourea to reduce the potential difference.^{34–38} Consequently, the intensive use of such toxic chemicals increases both the economic costs and challenges of the solution purification. In comparison, the ability of EDRR to enable the combination of different metals with distinct potentials is exceptional as it can be performed at room temperature without the need for any additional chemicals such as complexing agents.^{23–25} Earlier, EDRR studies have only investigated the formation of separate ultrafine particles (<1000 nm), while the further growth of the Ag/Zn bimetallic networks and dendrites has not been undertaken. Furthermore, as previously it has only been speculated that Ag and Zn existed in alloyed forms, based on energy-dispersive X-ray (EDS) spectroscopy analysis and electrochemical results, consequently, the exact identity of the associated crystalline phases have remained unverified.²⁵

Dealloying, or selective removal of less-noble components, is an effective approach to generate new attractive features like porous or dendritic structures for a broad range of applications such as sensors,³⁹ antimicrobial, ⁴⁰ and catalysis.⁴¹ The dealloying behavior of Ag/Zn binary alloys has been studied by several researchers; for example, Luo et al. have prepared bimodal nanoporous silver from an Ag₁₀Zn₉₀ precursor,²⁹ and the porosity evolution of Ag₂₅Zn₇₅ powder particles by chemical dealloying has been investigated by Bhushan et al.³⁰ In addition, Zhang et al. have fabricated nanoporous silver structures by dealloying Ag/Zn ribbons,³² whereas Li et al. have utilized Ag/Zn plates and the dealloying kinetics of Ag₂₅Zn₇₅ to produce nanoporous silver.^{31,33} Moreover, Kurowska-Tabor et al. have prepared porous thin silver films by the dealloying of Ag-Zn alloy films by traditional electrodeposition.³⁴ Nonetheless, all of these studies focused on the dealloying of Ag/Zn materials obtained by high-temperature processes (i.e., smelting–casting) or from a cyanide bath, while the Ag/Zn alloys obtained by EDRR have distinct properties, and their dealloying behavior is yet to be investigated. In general, dealloying can be undertaken by either chemical or electrochemical means. The chemical approach utilizes the spontaneous dissolution of the less-noble components into solutions, whereas electrochemical dealloying reactions are driven by the applied potential and therefore can be conducted under milder conditions.⁴² An electrochemical approach also has the additional advantage as it allows for the precise control of the dealloying process via the utilization of tailored operating potential or current. According to previous voltammetric studies, the oxidation potential of Zn (alloyed) is very close to pure silver within the Ag/Zn alloys produced by EDRR.²⁵ This suggests that the chemical dealloying of the Zn component would require a relatively aggressive medium like hydrochloric acid that has the potential to generate hazardous gas (e.g., HCl). Therefore, the current study suggests an alternative electrochemical approach to allow for a tailorable dealloying process for the produced Ag/Zn alloy under milder conditions with dilute sulfuric acid,

which has high availability as a byproduct in Zn production and a relatively low environmental impact. Additionally, the surface plasmonic resonance (SPR) of the dealloyed silver materials is studied to further highlight the potential for the direct synthesis of high value-added materials from conventional hydrometallurgical process-type solutions.

EXPERIMENTAL SECTION

Electrochemical experiments were performed with an IviumStat 24-bit CompactStat potentiostat (Ivium Technologies, The Netherlands) in a conventional three-electrode glass cell with a volume of 50 mL at room temperature. Glassy carbon (GC) plates (Alfa Aesar, U.S.A.) with one side exposed to provide a surface area of 1 cm² (square shape) were used as the working electrode, a platinum plate (ca. 9 cm², Pt wt % ≥ 99.5 wt % Pt, Kultakeskus Oy, Finland) comprised the counter electrode, and a saturated mercury–mercurous sulfate electrode (Hg/Hg₂SO₄, + 0.650 V vs standard hydrogen electrode (SHE), Mettler Toledo, Switzerland) was utilized as the reference electrode. Ag/Zn alloys were prepared on GC electrodes from a solution containing 65 g/L Zn (from ZnSO₄·7H₂O, ≥99%, VWR Chemicals, Belgium), 10 g/L H₂SO₄ (from concentrated H₂SO₄, 95–97%, EMD Millipore, Germany), and 20 ppm Ag (from AgNO₃, ≥99.0%, Sigma-Aldrich, USA) using up to 400 electrodeposition–redox replacement (EDRR) cycles. In general, a single EDRR cycle consists of two consecutive steps: (i) electrodeposition (ED), in which Zn is deposited at a deposition potential of E_1 for a deposition time of t_1 . This is immediately followed by step (ii) redox replacement (RR), where the external potential is disconnected for a preselected replacement time t_2 , during which the replacement reaction occurs spontaneously between Ag⁺ ions and deposited Zn because of the potential difference between to Ag⁺/Ag and Zn²⁺/Zn pairs. EDRR measurements with 10, 30, 50, 100, 150, 300, 600, and 800 cycles were conducted to investigate the growth mechanism of the Ag/Zn alloys. The subsequent electrochemical dealloying of the Ag/Zn alloys (after 400 EDRR cycles) was carried out in 10 g/L H₂SO₄ at −0.1 V (vs Hg/Hg₂SO₄). All the solutions were prepared with Millipore Milli-Q deionized water (DI water, ≥18 MΩ·cm). FactSage 8.1 thermodynamic software (Thermfact/CRCT, Canada & GTT-Technologies, Germany) was used for the calculation of the Ag-Zn binary phase diagram.

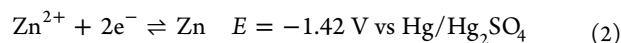
A Mira³ Tescan GM (Czech Republic) scanning electron microscope combined with energy-dispersive X-ray spectroscopy (EDS, ThermoFisher Scientific Ultradry EDS Detector, U.S.A.) was used for microstructural characterization and determination of sample compositions. Anodic linear sweep voltammetry (ALSV) was performed before and after dealloying in a 10 g/L H₂SO₄ solution at a scan speed of 5 mV/s in the potential range of −1.0 to +1.0 V (vs Hg/Hg₂SO₄). The crystalline phases of the Ag/Zn alloys (before dealloying) and the samples after dealloying were identified by X-ray diffraction (XRD, PANalytical X'Pert Pro Powder, Almelo, The Netherlands) using a Cu K α radiation source at a scan speed of 0.01°/min in the 2θ (°) range of 10–90° (acceleration potential 40 kV and current 40 mA) and the results were analyzed with HighScore 4.0+ software. Optical properties of the samples were characterized by ultraviolet–visible diffuse reflectance spectroscopy (UV/vis) using a Shimadzu UV-2600 UV/vis spectrometer. The absorbance spectra (A) were calculated based on the reflectance spectra (R) using eq 1:

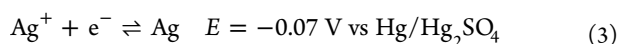
$$A = 100\% - R \quad (1)$$

where A is the absorbance (%), and R is the reflectance (%).

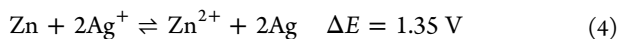
RESULTS AND DISCUSSION

The EDRR process involves the reduction of Zn²⁺ at an applied potential in the ED step using eq 2, and the reduction of Ag⁺ ions in the RR step is given in eq 3. The reduction potentials can be calculated using the Nernst equation.





The overall reaction during the RR step, which combines eqs 2 and 3, occurs spontaneously because of the potential difference (ΔE) between redox pairs Zn^{2+}/Zn and Ag^+/Ag



Earlier investigations have shown that particles (with a diameter < 1000 nm) of mixed Ag/Zn composition can be obtained with a short replacement time, whereas a long replacement time results in nearly pure Ag particles.²⁵ According to the binary alloy phase diagram of the Ag-Zn system (Figure S1 in the Supporting Information), various Ag/Zn intermetallic compounds are potentially stable at room temperature. Nevertheless, the crystalline compositions in the Ag/Zn mixtures by EDRR and the extent to which Zn and Ag exist either as independent phases or alloyed $\text{Ag}_x\text{Zn}_{1-x}$ phases are yet to be confirmed. Additionally, previous research has focused primarily on particle formation rather than the growth of more continuous alloys (i.e., using less than 30 EDRR cycles). As a result, this study focuses on the crystalline composition and the growth mechanism of the Ag/Zn alloys, formed through the application of a higher number of EDRR cycles up to a maximum of 800, as well as the dealloying mechanism involved in the creation Ag dendrites and how it affects their surface plasmon resonance behavior.

Ag/Zn Alloys by EDRR. Figure 1 illustrates typical potential–time transients: in this case, the initial 5 cycles

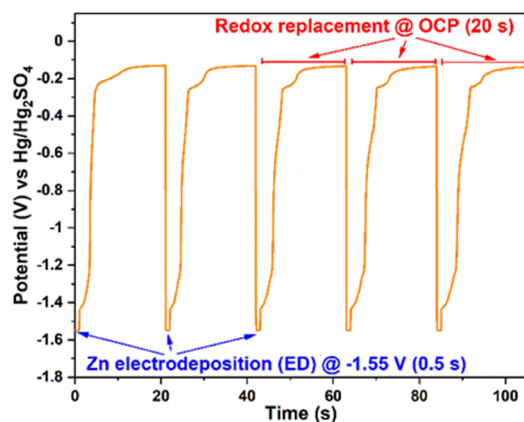


Figure 1. Typical potential–time profile of the initial five EDRR cycles in a solution containing 20 ppm Ag, 65 g/L Zn, and 10 g/L H_2SO_4 ($E = -1.55 \text{ V}$, $t_1 = 0.5 \text{ s}$, and $t_2 = 20 \text{ s}$).

from a total of 400 successive EDRR cycles. Zn was deposited at $E = -1.55 \text{ V}$ for 0.5 s (t_1) in the ED step, and this was immediately followed by an RR step, where the external electrical charge was disconnected for 20 s (t_2). In order to gain a more detailed understanding of the combined Ag/Zn material formation, relatively short t_1 times of 10 and 20 s were utilized. In addition, the effects of varying other parameters (E and t_2) were also investigated. Overall, six EDRR samples (S1–S6) were prepared, and the details of the experimental series are presented in Table 1, together with the related Ag/Zn compositions, as determined by EDS.

The morphologies of the as-prepared EDRR samples were observed by SEM, and as shown in Figure 2, deposits with different microstructures were obtained depending on the electrodeposition (t_1) and redox replacement (t_2) durations, as

Table 1. EDRR Experimental Details and Related Composition (EDS Results) of EDRR Samples before/after Electrochemical Dealloying (N.B. the Background Signal C and the Insignificant Level of O Present Are Excluded)

sample ID	$E(\text{V})$ vs Hg/ Hg_2SO_4	t_1 (s)	t_2 (s)	(Ag/Zn atom %)	
				as-prepared	after dealloying
S1	−1.55	0.5	10	73/27	94/6
S2	−1.55	0.5	20	83/17	96/4
S3	−1.65	0.5	10	28/72	95/5
S4	−1.65	0.5	20	77/23	95/5
S5	−1.55	1.0	10	15/85	94/6
S6	−1.55	1.0	20	68/32	96/4

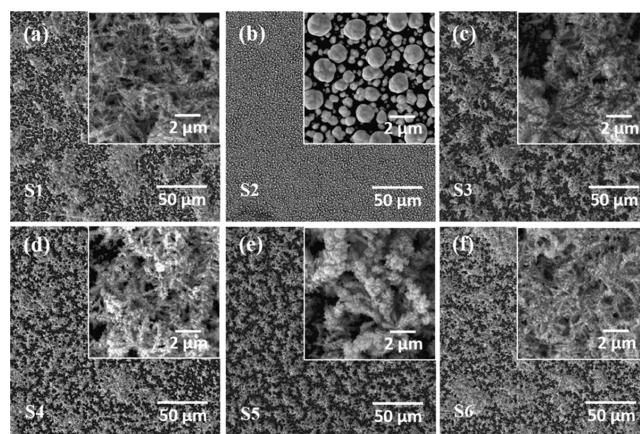


Figure 2. (a–f) SEM images of the as-prepared EDRR samples S1–S6 after 400 EDRR cycles in a solution containing 65 g/L Zn, 10 g/L H_2SO_4 , and 20 ppm of Ag with varying E , t_1 , and t_2 .

well as the initial deposition potential (E). Samples S1 (Figure 2a) and S3–S6 (Figure 2c–f) display pine treelike dendrites, whereas Sample S2 (Figure 2b) appears in the form of aggregated particles. As dendritic growth is significantly affected by mass-transfer conditions,⁴³ the reason for the difference in the behavior of Sample 2, when compared to all the other samples (S1 and S3–S6), can be explained by EDRR parameter selection: Sample S1 used a shorter replacement time, which is of insufficient duration for Ag^+ ions to migrate from the bulk solution, while for samples S3–S6, a higher amount of Zn was deposited in the ED step (because of either the longer deposition time or higher overpotential), and consequently, more Ag^+ ions were consumed in the RR step, resulting in mass-transfer limitations also with extended redox replacement times. Therefore, EDRR parameters, which lead to mass-transfer limitations and incomplete redox replacement (e.g., higher overpotentials, longer deposition times, or too short redox replacement times), were found to cause the dendritic growth of Ag/Zn alloys.

In addition, a smaller branch size was observed for the dendrites obtained with longer replacement times (Figure 2c (S3),e (S5)) than the samples with a short replacement time (Figure 2d (S4),f (S6)). The corresponding chemical composition of the deposits (in atom %, determined with EDS) is summarized in Table 1. Results show that for samples with the same deposition potential (E) and deposition time (t_1), the silver content increases within the deposits with longer replacement time (t_2) durations as more deposited zinc was replaced by silver, which correlates with the content of the

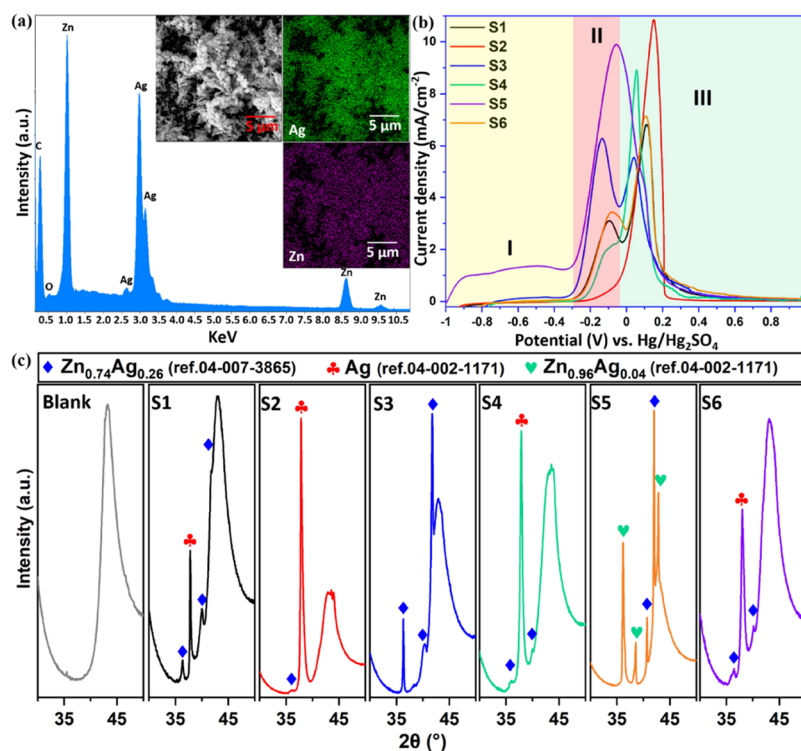


Figure 3. (a) Example of EDS spectra and mapping results of the EDRR sample (S5, $E = -1.55$ V, $t_1 = 1.0$ s, and $t_2 = 10$ s); (b) ALSV results, regions I, II, and III correspond with the dissolution of $\text{Zn}_{0.96}\text{Ag}_{0.04}$, $\text{Zn}_{0.76}\text{Ag}_{0.24}$, and Ag phases; and (c) XRD patterns of as-prepared EDRR samples.

noble metals in bimetallic particles determined earlier.^{23–25} In contrast, more negative E or longer t_1 results in higher Zn concentrations because of the higher production of zinc during the ED stages. For instance, samples S3 and S5 contain 72 and 85 atom % of Ag, respectively, while S1 has an Ag content of 27 atom %. Although the redox replacement reaction between the Ag^+ ions and Zn occurs at the solid/liquid interface, the diffusion of Ag atoms within the solid phase allows for the formation of a uniform elemental distribution in the deposits, as demonstrated by the EDS mapping results (e.g., S5) of the distribution of individual elements and the corresponding EDS spectra (Figure 3a). Moreover, as only a minor amount of Zn is deposited during an ED step in a single cycle (of total number of cycles 400), this allows for more complete diffusion of Ag during the RR steps in each cycle. Consequently, the even distribution of elements remained stable throughout the growth of larger structures when compared to the separate bimetallic particles observed previously,²⁵ and as a result, the behavior observed with EDRR growth is distinct from Ag/Zn dendrites produced by galvanic replacement using a prefabricated Zn plate in which clear local enrichment of individual elements was observed.⁴⁴

The Ag/Zn alloys were electrochemically analyzed with ALSV, as shown in Figure 3b, and it can be clearly observed that the results are dependent on the applied EDRR parameters. Dissolution of pure Zn and pure Ag in an H_2SO_4 solution normally comprises unimodal peaks located at ca. -1.45 and -0.1 V (vs $\text{Hg}/\text{Hg}_2\text{SO}_4$), respectively.^{19,25,45} In contrast, the distinctive behavior of the anodic peaks/current waves for samples prepared by EDRR can be attributed to the dissolution of specific Ag/Zn mixtures. From Figure 3b, it can be seen that the anodic dissolution of the deposits can be separated into three discrete regions (I–III). Furthermore,

because of the negative enthalpy of mixing (-3.43 kJ/mol) for Zn and Ag,³⁰ the potentials for the dissolution of Zn from the alloyed form is considerably higher than that of pure Zn, as presented in the ALSVs of the EDRR samples (ca. -1.0 V for S5 and ca. -0.3 V for the other samples *cf.* -1.42 V (vs $\text{Hg}/\text{Hg}_2\text{SO}_4$) for pure Zn). To further identify the crystalline phases dissolved in each region, the EDRR samples were also subjected to XRD analysis, as displayed in Figure 3c. For example, the anodic current wave in Region I was only present in S5, and based on the XRD analysis, this is due to Zn dissolution from a unique $\text{Zn}_{0.96}\text{Ag}_{0.04}$ alloy found to be only present in that sample. Anodic peaks/current waves appear with all samples when the potential is scanned to the more positive range found in Region (II). According to the XRD results, the dissolution of the Zn component from a $\text{Zn}_{0.76}\text{Ag}_{0.24}$ alloy occurs within this region. The major part of ALSV of S2 is located in Region III, and according to the Ag peak in the XRD pattern of S2, Region III is associated with the dissolution of the Ag phase. Furthermore, it can be seen from the XRD results that Ag peaks were not detected in samples S3 and S5, which suggests that all the Ag exists in an alloyed form within these particular samples because of the high Zn content. The formation of these two types of alloy phases might be related to their lattice structure, and the nominal pathway for alloy formation is presented in the Ag-Zn phase diagram (Figure S1). During RR, Ag atoms can diffuse into the Zn lattice and substitute for the original Zn atoms. Both $\text{Zn}_{0.76}\text{Ag}_{0.24}$ and $\text{Zn}_{0.96}\text{Ag}_{0.04}$ have a hexagonal closest packed (hcp) structure, which is similar to that of pure Zn, and therefore, the formation of such alloys is thermodynamically more favorable as no structural transformation takes place when compared to other alloy phases with different structures like body-centered-cubic (bcc). Overall, these results demon-

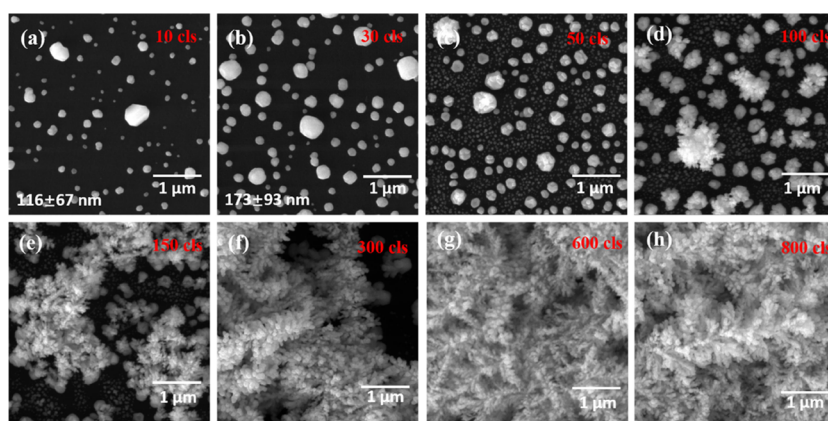


Figure 4. (a–h) SEM images of the GC working electrode surface after 10–800 EDRR cycles ($E = -1.55$ V, $t_1 = 1.0$ s, $t_2 = 20$ s).

strate for the first time that EDRR can be used to create and tailor the chemical composition, microstructure, and crystalline phases of Ag/Zn alloys through the variation of the related EDRR parameters.

SEM micrographs of the deposits by different EDRR cycles were examined to determine the nucleation and growth process of the Ag/Zn dendrites (Figure 4). The dendrite formation process mainly consists of initial nucleation followed by preferential growth in a certain direction. As can be seen from Figure 4a, separated particles with a rather inhomogeneous size distribution (116 ± 67 nm) were deposited with 10 EDRR cycles at different sites across the GC surface. These locations are believed to be activated nucleation sites, created by the distribution of the electric field,⁴⁶ and the size of particles varies as a consequence of the disparate surface energies at different active sites, which result in an uneven particle size distribution, that is, higher surface energies facilitate particle growth more than those of a lower magnitude.⁴⁷ Moreover, it has been previously demonstrated that pure Zn (formed by electrodeposition) appears as hexagonal flakes because of a lower thermodynamic free energy related to the exposed closest packed plane in hexagonal close-packed (hcp) metals,^{25,48,49} whereas the Ag/Zn particles formed by EDRR processes show distinct spherical morphologies. This observation is related to the mismatch of the atomic radii of Ag (covalent $r = 0.160$ nm) and Zn (covalent $r = 0.135$ nm),⁵⁰ which facilitates the congregation of Ag and Zn atoms as islands rather than growth as smooth layers. On the other hand, the possible simultaneous redissolution of Zn back to the electrolyte solution may also have an impact on the final morphology observed.

Although the particles continued to grow in a similar way when the number of EDRR cycles was increased from 10 to 30 (Figure 4a,b), a further increase in EDRR cycles to 50–100 or higher, the formation of dendritic structures starts to become more visible. Although the mechanisms of the dendrite growth via EDRR are yet to be completely understood, diffusion-limited aggregation (DLA) has previously been proposed to explain the growth of similar dendritic structures.^{43,51} Based on the results outlined here, the DLA mechanism can also be applied to explain the growth of Ag/Zn dendrites because of the presence of significant mass-transfer limitations within the system. With an increasing number of EDRR cycles, a concentration gradient of Zn is formed because of the depletion of related ions proximal to the electrode, which leads to the deviation of the electrode potential from

equilibrium and facilitates the Zn deposition at the tips of previously formed particles. Additionally, silver deposits also accumulate in the same area because of the redox replacement of the deposited Zn, and such a growth pattern promotes the initial stages of dendrite formation on the relatively larger particles when the number of EDRR cycles is increased to >50 (Figure 4c,d). As growth proceeds, the active sites undergo a shift to the tips of the dendritic structures, which—with the higher number of EDRR cycles—results in further enlargement of the dendritic formations with a higher number of branch-like features (Figure 4e,f). The nucleation-growth process of Ag/Zn dendrites via EDRR based on the SEM analysis is presented schematically in Figure 5.

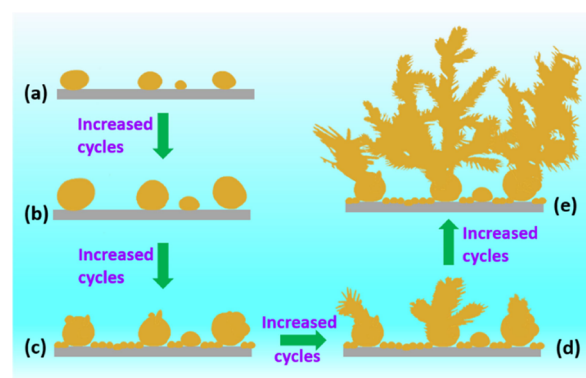


Figure 5. Schematic illustration of the growth process of Ag/Zn dendrites on the glassy carbon electrode. Ag/Zn particles are formed in the initial 10 cycles (a); particle size increases with 30 EDRR cycles (b); particles with a much smaller size (<100 nm) appear, and dendrite growth initiate on particles with a relatively large size (c); further growth of Ag/Zn dendrites (d, e).

Electrochemical Dealloying To Create Ag-Rich Surfaces. As the Ag/Zn alloys prepared by EDRR appear to have a different structure when compared to similar alloys that are prepared by high-temperature processes,^{38–42} a commonly used dealloying procedure was subsequently investigated to determine its effect on the materials prepared in the current study. According to the detailed investigation of the cyclic voltammograms in silver solutions without zinc, pure Ag can also be dissolved by H_2SO_4 solutions when the potential is more positive than -0.1 V (vs Hg/Hg_2SO_4).^{19,25} Although the dissolution potential of Zn (alloyed) is similar to that of Ag, the clear boundary between the Ag stripping peak and the Zn

(alloyed) stripping peak is observed and allows for selective Zn dissolution by the careful selection of the appropriate potential. In the case of the alloys produced by EDRR, the boundary of the Zn (alloyed) peak and the Ag peak in the ALSV curves (Figure 3b) is shifted to a slightly more positive value (ca. -0.05 V vs $\text{Hg}/\text{Hg}_2\text{SO}_4$). Such a difference is attributed to the fact that ALSV is a potentiodynamic method and when measurements are scanned from the negative direction to -0.1 V, a considerable amount of deposited Zn remains undissolved. This residual Zn in the deposits continued to dissolve when the potential was increased above -0.1 V and therefore resulted in the more positive potential of -0.05 V (vs $\text{Hg}/\text{Hg}_2\text{SO}_4$), which differentiates Regions II and III. Nonetheless, it should be noted that the dealloying of Ag/Zn is performed with a potentiostatic process at a constant potential. Consequently, the electrochemical dealloying of the Ag/Zn alloys was investigated at a constant potential of -0.1 V to selectively dissolve Zn (alloyed) and avoid silver dissolution.

Figure 6 shows the chronoamperometric curves recorded during the anodic dealloying of different samples, and as can be

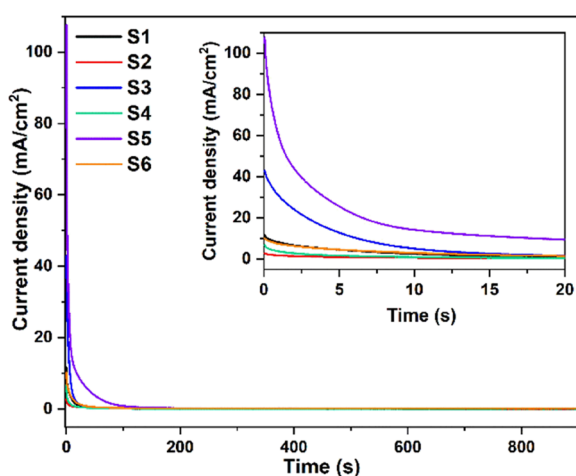


Figure 6. Chronoamperometric curves of as-prepared EDRR samples ($E = -0.1$ V (vs $\text{Hg}/\text{Hg}_2\text{SO}_4$), $t = 15$ min).

seen, the anodic currents clearly demonstrate the dissolution of the alloyed Zn from all samples. Most of the Zn (alloyed) was dissolved during the initial stages of the experiments as the current rapidly decays to a steady state close to 0 mA/cm^2 . This indicates that 15 min is sufficient for the dissolution of a majority of the alloyed Zn, whereas no Ag dissolution takes place at this potential. Furthermore, as current density is directly related to the Zn content of the EDRR samples, these results indicate that S5 has the highest Zn content as the dealloying process shows the highest level of anodic current density, a finding that was confirmed by the EDS analysis (Table 1).

Figure 7 shows the SEM micrographs of the EDRR samples after dealloying. As can be observed, there is a distinct change in the morphology when compared to the as-prepared samples. The major dealloying mechanisms proposed are closely related to the movement of metal atoms, in this case Zn and Ag, as a consequence of their intrinsic chemical reactivities. During the dealloying process, Zn dissolves from the metal lattice into the solution, which results in high-curvature clusters rich in Ag.^{46,52–54} This removal of Zn leads to surface roughening, whereas conversely, the curvature-driven aggregation of the

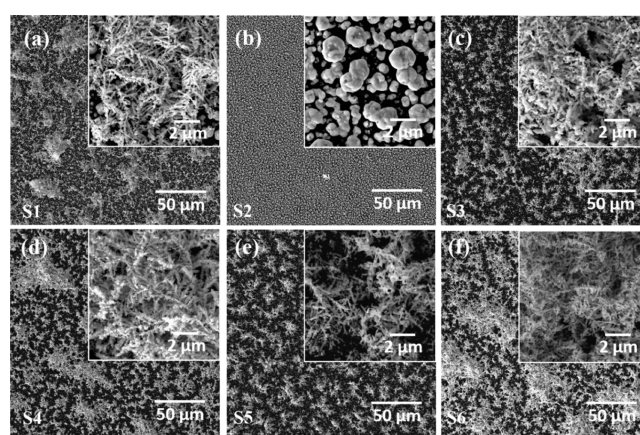


Figure 7. (a–f) SEM images of EDRR samples S1–S6 after electrochemical dealloying at -0.1 V (vs $\text{Hg}/\text{Hg}_2\text{SO}_4$) for 15 min.

remaining clusters of Ag atoms smoothens the surface. Figure 8 schematically illustrates a proposed mechanism to explain the

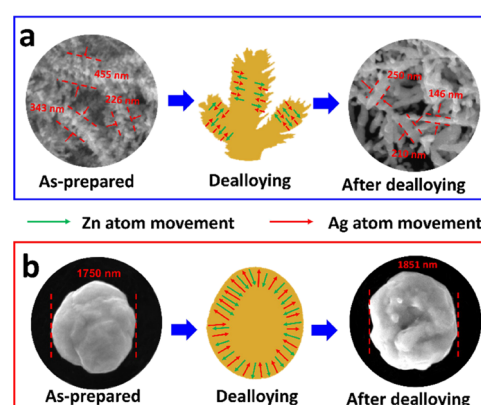


Figure 8. Schematic of the proposed dealloying mechanisms of (a) dendritic Ag/Zn structures and (b) Ag/Zn particles.

different morphologies obtained during the dealloying of dendritic structures and particles. As can be seen, within Ag/Zn dendrites, it is possible for Ag atoms to aggregate within the branch sections more easily because of significantly shorter distances when compared to those between Ag atoms in the Ag/Zn particles. Moreover, particles also have more compact structures that limit the diffusion of Ag, while dendrites have more open structures that favor surface diffusion. Consequentially, the as-prepared particles (Figure 2b) have relatively smooth surfaces, whereas the presence of pores within the particles is clear following the dealloying process. In contrast, as-prepared Ag/Zn dendrites (Figures 2a and 3c–f) have a branched morphology that becomes more pronounced, following electrochemical treatment with H_2SO_4 (Figure 7a,c–f). Furthermore, for dendrites with a relatively high Zn content, like those in S5 (Figure 2e), the deposits are denser prior to dealloying (S5, Figure 7e) because of the significant levels of Zn dissolution. Nevertheless, to further understand the dealloying mechanisms and kinetics, a more detailed investigation using techniques like in-situ synchrotron XRD analysis would be needed.⁵⁵

The corresponding chemical composition of the samples after dealloying (atom %, determined with EDS) is also summarized in Table 1. An increase in the quantitative Ag/Zn

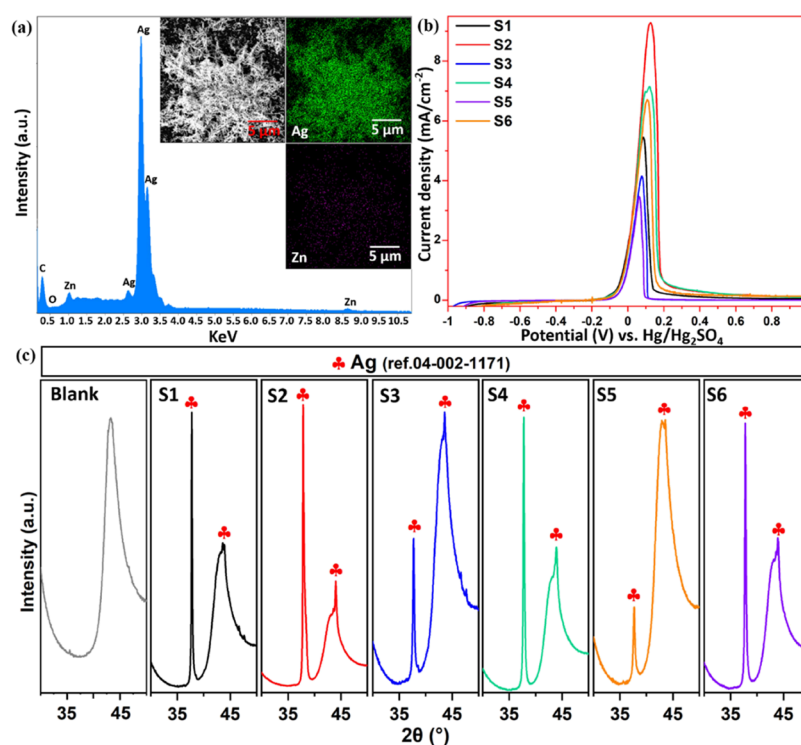


Figure 9. (a) Example of EDS spectra and mapping results (S5); (b) ALSV curves; and (c) XRD patterns of EDRR samples after electrochemical dealloying.

ratio in all the samples confirmed the selective dissolution of Zn during anodic dealloying. For example, the Ag/Zn ratio in S5 increased significantly from 15/85 to 94/6 after dealloying. Figure 9a shows the EDS spectrum and mapping results of S5 after dealloying. From the results, it is clear that the Zn peak is much reduced when compared with that of as-prepared S5 (Figure 3a), and the barely visible Zn signals on the mapping image are a direct confirmation of the significant decrease in the zinc content because of dealloying. The presence of the residual Zn (atom % $\leq 6\%$) is probably due to the mass-transfer limitations of Zn atoms within the solid phase during dealloying. The ALSVs of EDRR samples after dealloying are displayed in Figure 9b. In contrast to the as-prepared EDRR samples (Figure 3b), ALSVs of all the dealloyed samples appear as single-peak curves, and the potential where the anodic peaks initiate (ca. -0.1 V vs Hg/Hg₂SO₄) is close to the anodic peak within the cyclic voltammograms of a carbon electrode in the silver solution without Zn.^{25,45} This indicates the inconsequential nature of the remaining Zn within the crystal structure on the stripping process and further proves the extent of the selective Zn dissolution. Moreover, as the peak area directly correlates with the amount of Ag present on the surface of electrodes, a larger peak symbolizes a higher Ag content. Interestingly, when the other parameters remain unchanged, the anodic peaks of the dealloyed samples with a replacement time of 20 s have higher peaks than those with 10 s, highlighting the fact that more Zn is replaced with longer EDRR replacement times, resulting in higher amounts of Ag on the electrodes. Figure 9c shows the XRD results of the dealloyed samples, and clear differences can be seen when compared to the XRD patterns of the as-prepared samples (Figure 3c). Silver peaks from XRD were detected for all the dealloyed samples, while the peaks of Ag/Zn alloys

(Zn_{0.96}Ag_{0.04} and Zn_{0.76}Ag_{0.24}) disappeared, which clearly indicates the selective dissolution of Zn.

Optical Properties of Zn/Ag Alloys and Dealloyed Ag-rich Surfaces. Optically active surfaces that show (localized) surface plasmon resonance (LSPR) are intensively studied for different applications such as sensing and imaging,^{56,57} and Ag-based dendrites have created significant interest, for example, in sensing, as Ag is known to have strong SPR behavior.^{58,59} In order to test whether the Ag/Zn alloys and dealloyed surfaces developed here could have the potential for such applications in the future, they were characterized by UV/vis spectroscopy for LSPR. A spectrum of the GC substrate was also measured as a comparison, and all the related results are presented in Figure 10, with discernable differences seen between the spectra of different samples. The GC substrate shows an even absorption over the whole wavelength range because of its inherent black color, whereas only EDRR samples with a relatively high Ag content (S2 and S4) showed a weak absorption peak, present at ca. 315 nm (other samples show almost no detectable absorbance peaks). In contrast to the as-prepared EDRR samples, clear absorption bands due to LSPR can be seen on the spectra of all samples following the dealloying process.

LSPR is known to be closely related to the morphology, size, and dielectric environment of silver materials,⁶⁰ and according to the Mie theory, spherical Ag particles show a single absorption band, while two or more peaks are usually observed with anisotropic materials.⁶⁰ In the current study, the dendritic samples after dealloying (S1 and S3–S6) show two absorbance peaks at ca. 315 and 360 nm. Dual-peak surface plasmon resonance has also been reported within dendritic silver structures produced by electrodeposition,⁶¹ galvanic replacement,⁶² and chemical etching,⁶³ although the wavenumbers of the peaks here are different because of the difference in

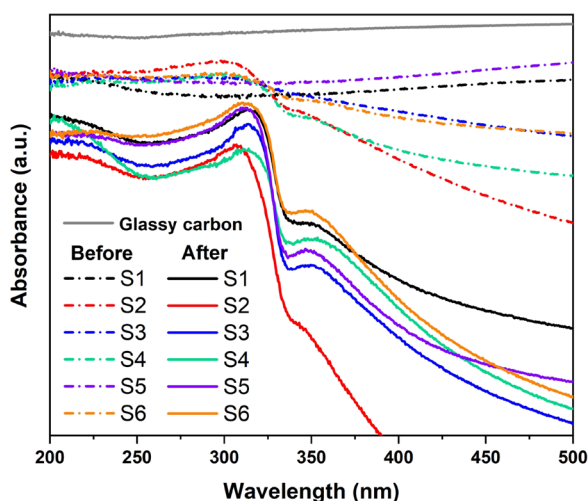


Figure 10. UV-vis spectra of a glassy carbon substrate, as-prepared EDRR samples, and EDRR samples after dealloying.

properties like morphology and dielectric environment. On the other hand, the UV/vis spectra of sample S2 are close to a single peak at ca. 310 nm. The absorption-shoulder-peak at ca. 360 nm is almost invisible, possibly due to its distinct morphology (porous particles) when compared to other samples. The enhanced SPR behavior of the dealloyed *cf.* the as-prepared samples suggests that dealloying is a powerful approach to fully exploit the Ag/Zn alloys prepared by EDRR for potential applications. Moreover, the change in the SPR behavior of dealloyed samples from a single-peak to dual-peak shows that a combination of EDRR and dealloying can be used to tailor the optical properties of the surfaces simply by controlling the operating parameters. For example, the selection of Ag/Zn growth conditions in EDRR that favor dendrites, that is, mass-transfer limitations (shorter redox replacement times, higher overpotentials, or longer deposition times), followed by dealloying (selective Zn dissolution), leads to Ag-rich dendrites with clear dual-peak SPR behavior, whereas the utilization of EDRR parameters that favor spherical particles, surfaces with single peak would be achieved.

CONCLUSIONS

Ag/Zn alloys have been successfully prepared using the EDRR method from a simulated Zn hydrometallurgical process solution containing a high Zn concentration (65 g/L) and minimal silver content (20 ppm). The presence of an alloyed form of Ag and Zn in the EDRR deposits (previously only hypothesized based on voltammetric studies and EDS results) has been confirmed for the first time by the combination of XRD and ALSV. By controlling EDRR parameters such as deposition potential, deposition time, and redox replacement time, Ag/Zn alloys with different morphologies, that include dendritic structures and aggregated particles, were obtained. Detailed SEM studies further revealed the nucleation and growth mechanism of Ag/Zn particles to the highly dendritic microstructures that result from an increased number of EDRR cycles. The dealloying behavior of the prepared Ag/Zn alloys was also investigated and a majority of the Zn in the Ag/Zn alloys was selectively dissolved in a 10 g/L H₂SO₄ solution at a potential of -0.1 V (vs Hg/Hg₂SO₄) after 15 min. Compared to the as-prepared Ag/Zn alloys, dealloyed surfaces showed distinct chemical compositions, crystalline phases, morphology,

and optical properties. Enhanced SPR was observed on the UV/vis spectra of dealloyed samples, and moreover, by tailoring the EDRR parameters, the optical properties of the dealloyed samples are tunable from single-peak to dual-peak SPR.

Overall, these findings demonstrate the versatile nature of the EDRR method, which allows for the more sustainable creation of distinct Ag/Zn alloys at room temperature without the addition of any complexing agents from the otherwise underutilized silver present in Zn process solutions. Furthermore, the distinct optical properties of the dealloyed Ag-rich dendrites further prove the significant potential of the combined EDRR-dealloying protocol.

ASSOCIATED CONTENT

Supporting Information

The Supporting Information is available free of charge at <https://pubs.acs.org/doi/10.1021/acssuschemeng.2c00284>.

Ag-Zn binary phase diagram (PDF)

AUTHOR INFORMATION

Corresponding Author

Mari Lundström – Department of Chemical and Metallurgical Engineering, School of Chemical Engineering, Aalto University, 02150 Espoo, Finland; Email: mari.lundstrom@aalto.fi

Authors

Zulin Wang – Department of Chemical and Metallurgical Engineering, School of Chemical Engineering, Aalto University, 02150 Espoo, Finland; orcid.org/0000-0002-2234-7983

Kirsi Yliniemi – Department of Chemistry and Materials Science, School of Chemical Engineering, Aalto University, 02150 Espoo, Finland; orcid.org/0000-0003-2536-388X

Eeva-Leena Rautama – Department of Chemistry and Materials Science, School of Chemical Engineering, Aalto University, 02150 Espoo, Finland

Pyry-Mikko Hannula – Department of Chemical and Metallurgical Engineering, School of Chemical Engineering, Aalto University, 02150 Espoo, Finland; orcid.org/0000-0001-9844-2234

Benjamin P. Wilson – Department of Chemical and Metallurgical Engineering, School of Chemical Engineering, Aalto University, 02150 Espoo, Finland; orcid.org/0000-0002-2874-6475

Complete contact information is available at: <https://pubs.acs.org/doi/10.1021/acssuschemeng.2c00284>

Notes

The authors declare no competing financial interest. The data underlying this study are openly available in Zenodo at doi:10.5281/zenodo.5561034.

ACKNOWLEDGMENTS

Academy of Finland project (GoldTail (319691) BW) and EARMetal (339979, ML, KY) are greatly acknowledged for funding this research. The RawMatTERS Finland Infrastructure (RAMI) funded by the Academy of Finland and based at Aalto University is also acknowledged. In addition, Zulin Wang would like to acknowledge the financial support from the Chinese Scholarship Council (CSC). The authors

would also like to thank Min Chen for his valuable suggestion and discussion.

REFERENCES

- (1) Park, H.; Choi, J.; Kim, H.; Hwang, E.; Ha, D.-H.; Ahn, S. H.; Kim, S.-K. AgIn Dendrite Catalysts for Electrochemical Reduction of CO₂ to CO. *Appl. Catal., B* **2017**, *219*, 123–131.
- (2) Yu, H.; He, Y. Seed-Assisted Synthesis of Dendritic Au–Ag Bimetallic Nanoparticles with Chemiluminescence Activity and Their Application in Glucose Detection. *Sens. Actuators, B* **2015**, *209*, 877–882.
- (3) Oseni, S. O.; Tessema Mola, G. Bimetallic Nanocomposites and the Performance of Inverted Organic Solar Cell. *Composites, Part B* **2019**, *172*, 660–665.
- (4) Padmos, J. D.; Langman, M.; MacDonald, K.; Comeau, P.; Yang, Z.; Filiaggi, M.; Zhang, P. Correlating the Atomic Structure of Bimetallic Silver–Gold Nanoparticles to Their Antibacterial and Cytotoxic Activities. *J. Phys. Chem. C* **2015**, *119*, 7472–7482.
- (5) Sverdrup, H.; Koca, D.; Ragnarsdottir, K. V. Investigating the Sustainability of the Global Silver Supply, Reserves, Stocks in Society and Market Price Using Different Approaches. *Resour. Conserv. Recycl.* **2014**, *83*, 121–140.
- (6) Norouzi, A.; Adeli, M.; Zakeri, A. An Innovative Hydrometallurgical Process for the Production of Silver Nanoparticles from Spent Silver Oxide Button Cells. *Sep. Purif. Technol.* **2020**, *248*, No. 117015.
- (7) Swain, B.; Shin, D.; Joo, S. Y.; Ahn, N. K.; Lee, C. G.; Yoon, J.-H. Selective Recovery of Silver from Waste Low-Temperature Co-Fired Ceramic and Valorization through Silver Nanoparticle Synthesis. *Waste Manage.* **2017**, *69*, 79–87.
- (8) Ganesan, R.; Narasimhalu, P.; Joseph, A. I. J.; Pugazhendhi, A. Synthesis of Silver Nanoparticle from X-Ray Film and Its Application in Production of Biofuel from Jatropha Oil. *Int. J. Energy Res.* **2021**, *45*, 17378–17388.
- (9) Wang, W.; Li, R.; Yuan, T.; Zhu, X.; Li, H.; Lin, W.; Li, L. Effects of Ag⁺ in Diaphragm Electrolysis on Oxygen Evolution and Corrosion Behaviors of Pb and PbAg Anodes. *Hydrometallurgy* **2020**, *192*, No. 105254.
- (10) Crundwell, F.; Moats, M.; Ramachandran, V.; Robinson, T.; Davenport, W. G. *Extractive Metallurgy of Nickel, Cobalt and Platinum Group Metals*; Elsevier: 2011, pp. 393–535.
- (11) Davenport, W. G.; King, M. J.; Schlesinger, M. E.; Biswas, A. K. *Extractive Metallurgy of Copper*; Elsevier: 2002, pp. 415–427.
- (12) Torres, R.; Lapidus, G. T. Platinum, Palladium and Gold Leaching from Magnetite Ore, with Concentrated Chloride Solutions and Ozone. *Hydrometallurgy* **2016**, *166*, 185–194.
- (13) Yliniemi, K.; Wang, Z.; Korolev, I.; Hannula, P.; Halli, P.; Lundström, M. Effect of Impurities in Precious Metal Recovery by Electrodeposition-Redox Replacement Method from Industrial Side-Streams and Process Streams. *ECS Trans.* **2018**, *85*, 59.
- (14) Halli, P.; Wilson, B. P.; Hailemariam, T.; Latostenmaa, P.; Yliniemi, K.; Lundström, M. Electrochemical Recovery of Tellurium from Metallurgical Industrial Waste. *J. Appl. Electrochem.* **2020**, *50*, 1–14.
- (15) Halli, P.; Elomaa, H.; Wilson, B. P.; Yliniemi, K.; Lundström, M. Improved Metal Circular Economy-Selective Recovery of Minor Ag Concentrations from Zn Process Solutions. *ACS Sustainable Chem. Eng.* **2017**, *5*, 10996–11004.
- (16) Altinkaya, P.; Wang, Z.; Korolev, I.; Hamuyuni, J.; Haapalainen, M.; Kolehmainen, E.; Yliniemi, K.; Lundström, M. Leaching and Recovery of Gold from Ore in Cyanide-Free Glycine Media. *Miner. Eng.* **2020**, *158*, No. 106610.
- (17) Korolev, I.; Spatharitis, S.; Yliniemi, K.; Wilson, B. P.; Abbott, A. P.; Lundström, M. Mechanism of Selective Gold Extraction from Multi-Metal Chloride Solutions by Electrodeposition-Redox Replacement. *Green Chem.* **2020**, *22*, 3615–3625.
- (18) Halli, P.; Heikkinen, J. J.; Elomaa, H.; Wilson, B. P.; Jokinen, V.; Yliniemi, K.; Franssila, S.; Lundström, M. Platinum Recovery from Industrial Process Solutions by Electrodeposition-Redox Replacement. *ACS Sustainable Chem. Eng.* **2018**, *6*, 14631–14640.
- (19) Wang, Z.; Halli, P.; Hannula, P.; Liu, F.; Wilson, B. P.; Yliniemi, K.; Lundström, M. Recovery of Silver from Dilute Effluents via Electrodeposition and Redox Replacement. *J. Electrochem. Soc.* **2019**, *166*, E266.
- (20) Korolev, I.; Altinkaya, P.; Halli, P.; Hannula, P.-M.; Yliniemi, K.; Lundström, M. Electrochemical Recovery of Minor Concentrations of Gold from Cyanide-Free Cupric Chloride Leaching Solutions. *J. Cleaner Prod.* **2018**, *186*, 840–850.
- (21) Korolev, I.; Altinkaya, P.; Haapalainen, M.; Kolehmainen, E.; Yliniemi, K.; Lundström, M. Electro-Hydrometallurgical Chloride Process for Selective Gold Recovery from Refractory Telluride Gold Ores: A Mini-Pilot Study. *Chem. Eng. J.* **2022**, *429*, No. 132283.
- (22) Korolev, I.; Yliniemi, K.; Lindgren, M.; Carpén, L.; Lundström, M. Performance-Based Selection of the Cathode Material for the Electrodeposition-Redox Replacement Process of Gold Recovery from Chloride Solutions. *Metall. Mater. Trans. B* **2021**, 3107.
- (23) Yliniemi, K.; Nguyen, N. T.; Mohajernia, S.; Liu, N.; Wilson, B. P.; Schmuki, P.; Lundström, M. A Direct Synthesis of Platinum/Nickel Co-Catalysts on Titanium Dioxide Nanotube Surface from Hydrometallurgical-Type Process Streams. *J. Cleaner Prod.* **2018**, *201*, 39–48.
- (24) Hannula, P.-M.; Pletincx, S.; Janas, D.; Yliniemi, K.; Hubin, A.; Lundström, M. Controlling the Deposition of Silver and Bimetallic Silver/Copper Particles onto a Carbon Nanotube Film by Electrodeposition-Redox Replacement. *Surf. Coat. Technol.* **2019**, *374*, 305–316.
- (25) Wang, Z.; Hannula, P.-M.; De, S.; Wilson, B. P.; Vapaavuori, J.; Yliniemi, K.; Lundström, M. Controllable Production of Ag/Zn and Ag Particles from Hydrometallurgical Zinc Solutions. *ACS Sustainable Chem. Eng.* **2021**, *9*, 8186–8197.
- (26) Zhu, L.; Liu, X.; Wang, X.; Meng, X. Evaluation of Photocatalytic Selectivity of Ag/Zn Modified Molecularly Imprinted TiO₂ by Multiwavelength Measurement. *Sci. Total Environ.* **2020**, *703*, No. 134732.
- (27) Reyes-Vidal, Y.; Suarez-Rojas, R.; Ruiz, C.; Torres, J.; Tălu, Ș.; Méndez, A.; Trejo, G. Electrodeposition, Characterization, and Antibacterial Activity of Zinc/Silver Particle Composite Coatings. *Appl. Surf. Sci.* **2015**, *342*, 34–41.
- (28) Hatsukade, T.; Kuhl, K. P.; Cave, E. R.; Abram, D. N.; Feaster, J. T.; Jongerius, A. L.; Hahn, C.; Jaramillo, T. F. Carbon Dioxide Electroreduction Using a Silver–Zinc Alloy. *Energy Technol.* **2017**, *5*, 955–961.
- (29) Luo, J.; Han, P.; Dan, Z.; Qin, F.; Tang, T.; Dong, Y. Bimodal Nanoporous Silver Fabricated from Dual-Phase Ag₁₀Zn₉₀ Precursor via Electrochemical Dealloying for Direct Ammonia-Borane Electro-oxidation. *Microporous Mesoporous Mater.* **2020**, *308*, No. 110532.
- (30) Bhushan, B.; Murty, B. S.; Mondal, K. Dealloying Kinetics and Mechanism of Porosity Evolution in Mechanically Alloyed Ag₂₅Zn₇₅ Powder Particles. *Corros. Sci.* **2018**, *139*, 155–162.
- (31) Li, Z. Q.; Li, B. Q.; Qin, Z. X.; Lu, X. Fabrication of Porous Ag by Dealloying of Ag–Zn Alloys in H₂SO₄ Solution. *J. Mater. Sci.* **2010**, *45*, 6494–6497.
- (32) Zhang, C.; Sun, J.; Xu, J.; Wang, X.; Ji, H.; Zhao, C.; Zhang, Z. Formation and Microstructure of Nanoporous Silver by Dealloying Rapidly Solidified Zn–Ag Alloys. *Electrochim. Acta* **2012**, *63*, 302–311.
- (33) Li, Z.; Wang, D.; Li, B.; Lu, X. The Dealloying Kinetics of Ag₂₅Zn₇₅ in 0.1 M H₂SO₄. *J. Electrochem. Soc.* **2010**, *157*, K223.
- (34) Kurowska-Tabor, E.; Gawlak, K.; Hnida, K.; Jaskula, M.; Sulka, G. D. Synthesis of Porous Thin Silver Films and Their Application for Hydrogen Peroxide Sensing. *Electrochim. Acta* **2016**, *213*, 811–821.
- (35) Roy, S. Controlled Potential Deposition of Silver-Zinc Alloys. *Surf. Technol.* **1978**, *6*, 191–201.
- (36) Roy, S.; Banerjee, T. Current Efficiencies of Ag-Zn Alloys under Potentiostatic Conditions. *Surf. Technol.* **1977**, *5*, 43–48.
- (37) Roy, S.; Banerjee, T. Phase Transformations in Electrolytic Silver-Zinc Alloys. *Electrodeposition Surf. Treat.* **1975**, *3*, 289–305.

- (38) de Oliveira, G. M.; Carlos, I. A. Silver–Zinc Electrodeposition from a Thiourea Solution with Added EDTA or HEDTA. *Electrochim. Acta* **2009**, *54*, 2155–2163.
- (39) Zhao, P.; Liu, H.; Zhang, L.; Zhu, P.; Ge, S.; Yu, J. Paper-Based SERS Sensing Platform Based on 3D Silver Dendrites and Molecularly Imprinted Identifier Sandwich Hybrid for Neonicotinoid Quantification. *ACS Appl. Mater. Interfaces* **2020**, *12*, 8845–8854.
- (40) Thukkaram, M.; Cools, P.; Nikiforov, A.; Rigole, P.; Coenye, T.; Van Der Voort, P.; Du Laing, G.; Vercruyse, C.; Declercq, H.; Morent, R.; De Wilde, L.; De Baets, P.; Verbeken, K.; De Geyter, N. Antibacterial Activity of a Porous Silver Doped TiO₂ Coating on Titanium Substrates Synthesized by Plasma Electrolytic Oxidation. *Appl. Surf. Sci.* **2020**, *500*, No. 144235.
- (41) Abeyweera, S. C.; Yu, J.; Perdew, J. P.; Yan, Q.; Sun, Y. Hierarchically 3D Porous Ag Nanostructures Derived from Silver Benzenethiolate Nanoboxes: Enabling CO₂ Reduction with a Near-Unity Selectivity and Mass-Specific Current Density over 500 A/g. *Nano Lett.* **2020**, *20*, 2806–2811.
- (42) Song, T.; Yan, M.; Qian, M. The Enabling Role of Dealloying in the Creation of Specific Hierarchical Porous Metal Structures—A Review. *Corros. Sci.* **2018**, *134*, 78–98.
- (43) Zuo, Y.; Wang, K.; Pei, P.; Wei, M.; Liu, X.; Xiao, Y.; Zhang, P. Zinc Dendrite Growth and Inhibition Strategies. *Mater. Today Energy* **2021**, *20*, No. 100692.
- (44) Chen, J.; Davies, J. J.; Goodfellow, A. S.; Hall, S. M. D.; Lancaster, H. G.; Liu, X.; Rhodes, C. J.; Zhou, W. Growth Mechanisms of Ag and Cu Nanodendrites via Galvanic Replacement Reactions. *Prog. Nat. Sci.: Mater. Int.* **2021**, *31*, 141–151.
- (45) Wang, Z.; Peng, C.; Yliniemi, K.; Lundström, M. Recovery of High-Purity Silver from Spent Silver Oxide Batteries by Sulfuric Acid Leaching and Electrowinning. *ACS Sustainable Chem. Eng.* **2020**, *8*, 15573–15583.
- (46) Gupta, A.; Srivastava, C. Nucleation and Growth Mechanism of Tin Electrodeposition on Graphene Oxide: A Kinetic, Thermodynamic and Microscopic Study. *J. Electroanal. Chem.* **2020**, *861*, No. 113964.
- (47) Guo, L.; Searson, P. C. On the Influence of the Nucleation Overpotential on Island Growth in Electrodeposition. *Electrochim. Acta* **2010**, *55*, 4086–4091.
- (48) Sato, R. Crystal Growth of Electrodeposited Zinc: An Electron Diffraction and Electron Microscopic Study. *J. Electrochem. Soc.* **1959**, *106*, 206.
- (49) Zheng, J.; Zhao, Q.; Tang, T.; Yin, J.; Quilty, C. D.; Renderos, G. D.; Liu, X.; Deng, Y.; Wang, L.; Bock, D. C.; Jaye, C.; Zhang, D.; Takeuchi, E. S.; Takeuchi, K. J.; Marschilok, A. C.; Archer, L. A. Reversible Epitaxial Electrodeposition of Metals in Battery Anodes. *Science* **2019**, *366*, 645–648.
- (50) Slater, J. C. Atomic Radii in Crystals. *J. Chem. Phys.* **1964**, *41*, 3199–3204.
- (51) Wang, K.; Xiao, Y.; Pei, P.; Liu, X.; Wang, Y. A Phase-Field Model of Dendrite Growth of Electrodeposited Zinc. *J. Electrochem. Soc.* **2019**, *166*, D389.
- (52) Sieradzki, K. Curvature Effects in Alloy Dissolution. *J. Electrochem. Soc.* **1993**, *140*, 2868.
- (53) Chen, Q.; Sieradzki, K. Mechanisms and Morphology Evolution in Dealloying. *J. Electrochem. Soc.* **2013**, *160*, C226.
- (54) Erlebacher, J. An Atomistic Description of Dealloying: Porosity Evolution, the Critical Potential, and Rate-Limiting Behavior. *J. Electrochem. Soc.* **2004**, *151*, C614.
- (55) Song, T.; Schmid-Fetzer, R.; Yan, M.; Qian, M. Near Room-Temperature Formation of Cu₃Sn: In-Situ Synchrotron X-Ray Diffraction Characterization and Thermodynamic Assessments of Its Nucleation. *Acta Mater.* **2021**, *213*, No. 116894.
- (56) Stockman, M. I. Nanoplasmonic Sensing and Detection. *Science* **2015**, *348*, 287–288.
- (57) Steiner, G. Surface Plasmon Resonance Imaging. *Anal. Bioanal. Chem.* **2004**, *379*, 328–331.
- (58) Wang, Z.; Cheng, Z.; Singh, V.; Zheng, Z.; Wang, Y.; Li, S.; Song, L.; Zhu, J. Stable and Sensitive Silver Surface Plasmon Resonance Imaging Sensor Using Trilayered Metallic Structures. *Anal. Chem.* **2014**, *86*, 1430–1436.
- (59) Gao, C.; Lu, Z.; Liu, Y.; Zhang, Q.; Chi, M.; Cheng, Q.; Yin, Y. Highly Stable Silver Nanoplates for Surface Plasmon Resonance Biosensing. *Angew. Chem. Int. Ed.* **2012**, *51*, 5629–5633.
- (60) Hergert, W.; Wriedt, T. *The Mie Theory: Basics and Applications*; Springer: 2012, pp. 111–122
- (61) Mandke, M. V.; Han, S.-H.; Pathan, H. M. Growth of Silver Dendritic Nanostructures via Electrochemical Route. *CrystEngComm* **2012**, *14*, 86–89.
- (62) Rezaei, S.; Landarani–Isfahani, A.; Moghadam, M.; Tangestaninejad, S.; Mirkhani, V.; Mohammadpoor–Baltork, I. Development of a Novel Bi-Enzymatic Silver Dendritic Hierarchical Nanostructure Cascade Catalytic System for Efficient Conversion of Starch into Gluconic Acid. *Chem. Eng. J.* **2019**, *356*, 423–435.
- (63) Zong, R.-L.; Zhou, J.; Li, Q.; Du, B.; Li, B.; Fu, M.; Qi, X.-W.; Li, L.-T.; Buddhudu, S. Synthesis and Optical Properties of Silver Nanowire Arrays Embedded in Anodic Alumina Membrane. *J. Phys. Chem. B* **2004**, *108*, 16713–16716.

Editor-in-Chief
Prof. Christopher W. Jones
Georgia Institute of Technology, USA

Open for Submissions

pubs.acs.org/jacsau

ACS Publications
Most Trusted. Most Cited. Most Read.